



1 CFD Study of Aquatic Thrust Generation by an Octopus-like Arm
2 Under Intense Prescribed Deformations

3 Asimina Kazakidi^{1a}, Dimitris P. Tsakiris^a, Dionysios Angelidis^b, Fotis Sotiropoulos^b,
4 John A. Ekaterinaris^{c,d}

5 ^a*Institute of Computer Science, Foundation for Research & Technology - Hellas (FORTH), 70013 Heraklion, Crete, Greece*

6 ^b*St. Anthony Falls Laboratory, University of Minnesota, Minneapolis, MN, 55455-0116, USA*

7 ^c*Department of Aerospace Engineering, Embry-Riddle Aeronautical University, Daytona Beach, FL, 32114, USA*

8 ^d*Institute of Applied & Computational Mathematics, FORTH, 70013 Heraklion, Crete, Greece*

9 **Abstract**

10 The complexity in structure and locomotion of cephalopods, such as the octopus, poses difficulties in modeling and
11 simulation. Their slender arms, being highly agile and dexterous, often involve intense deformations, which are hard
12 to simulate accurately, while simultaneously ensuring numerical stability and low diffusion of the transient motion
13 results. Within the Immersed-Boundary framework, this paper focuses on an arm geometry performing prescribed
14 motions that reflect octopus locomotion. The method is compared with a Finite-Volume numerical approach to deter-
15 mine the mesh requirements that must be employed for sufficiently capturing, not only the near wall viscous flow, but
16 also the off-body vortical flow field in intense forced motions. The objective is to demonstrate and exploit the gener-
17 ality of the immersed boundary approach to complex numerical simulations of deforming geometries. Incorporation
18 of arm deformation was found to increase the output thrust of a single-arm system. It was further found that sculling
19 motion combined with arm undulations provides an effective propulsive scheme for an octopus-like arm.

20 *Keywords:* Computational fluid dynamics (CFD), aquatic locomotion, biological propulsion, large deformations,
21 immersed boundary method

¹Corresponding author: Email: kazakidi@ics.forth.gr; Tel.: +30 2810 391695; Fax: +30 2810 391601.

1. Introduction

The appendages of cephalopods (i.e., the arms and tentacles of squids and cuttlefish, the octopus arms, and the nautilus tentacles) are elongated muscular structures, composed of a tight 3D musculature maintaining constant volume despite large deformations (termed muscular hydrostats [1]). Cephalopods may use their arms and, for squids and cuttlefish, also their fins, to perform a large repertoire of movements and behaviors [2, 3]. We are interested in investigating the individual role of octopus arms in aquatic locomotion and the generated hydrodynamic forces, which have not been explored in detail. Studies of fish swimming (as well as of bird flight) have shown that various marine animals, as well as birds, are able to exploit and control perturbations found in the surrounding fluid (e.g. vortices and eddies), in order to limit the levels of energy consumption and augment the produced thrust [4, 5, 6, 7, 8, 9, 10, 11, 12, 13, 14]. This work aims to investigate the flow dynamics around intense octopus-like motions, in an attempt to shed light on the underlying mechanisms and the energetics of cephalopod swimming.

The main difficulty in numerical flow simulations around time-varying geometries involving intense motions, is that the computational grid must deform over time, following the motion of the body (body-fitted methods). Finite volume (FV) body conforming methods include mesh deformation techniques that fulfill the geometric conservation requirement [15, 16] for small deformations and can provide high-fidelity results. These methods have the advantage of capturing in great detail the boundary layer around the swimming body and can simulate flows at high Reynolds numbers. They also allow for a direct application of the boundary conditions on the moving body. However, the mesh generation is demanding and the computational cost, for methods involving moving mesh or re-meshing strategies at every time step during a simulation, can be significantly high. For large grid deformations, in particular, re-meshing may affect the stability and accuracy of the numerical scheme [15].

Fixed-grid numerical methods, on the other hand, have attracted much attention in recent years, particularly for complex fluid-structure interaction problems. The advantage of these methods is their efficiency in handling arbitrarily large deformations with relatively low computational cost, since no mesh-updating strategies are involved. Instead, the effect of the moving body is defined on a fixed computational domain through the addition of external forces in the governing equations of motion. The external force field must satisfy the no-slip condition of the fluid on the moving solid body. Some of the challenges that fixed-grid methods face are related to the accurate definition of the

48 moving body with respect to the fixed domain, and the successful application of the boundary conditions. The best-
49 known fixed-grid numerical method for moving bodies is the immersed boundary method (IBM) of Peskin (1972)
50 [17, 18], where a delta function is implemented for the distribution of the surface forces over several mesh nodes
51 around the moving body, in order to avoid numerical instabilities. This produces smearing of the interface and, hence,
52 immersed boundary methods require increased spatial resolution around the moving body. Further developments in
53 this approach are limited to solutions with moderate Reynolds numbers [19, 20]. Approaches that overcome these
54 shortcomings are the immersed interface method (IIM) [21] and the hybrid Cartesian/immersed boundary method
55 (HCIB) [22, 23, 24, 25].

56 Here, we focused on the use of an immersed-boundary HCIB approach [24, 25] to implement and study prescribed
57 deformations, because of its robustness and handling capability. The mesh requirements for capturing the boundary
58 layer and evaluate accurately the generated hydrodynamic forces were determined by comparing the method with
59 a finite-volume approach [26, 27]. This investigation lies within a well-known field of research on aquatic animal
60 locomotion, on which there exists a considerable amount of literature [4, 5, 6, 7, 8, 9, 10, 11, 12, 13, 14, 28]. Nev-
61 ertheless, many questions on aquatic swimming remain unanswered, in particular for cephalopods. This work seeks
62 to study the flow dynamics around intense octopus-like motions, utilizing computational fluid dynamic techniques on
63 time-varying arm geometries performing prescribed motions. It also aims to demonstrate and exploit the generality
64 of the immersed boundary approach to complex numerical simulations of such geometries. Incorporation of arm de-
65 formation was found to increase the output thrust of a single-arm system. It was further found that sculling motion
66 combined with arm undulation is an effective propulsive scheme for an octopus-like arm.

67 The remainder of the paper is organized as follows: Section 2 discusses the arm kinematics and the numerical
68 frameworks utilized; Section 3 presents flow simulations around an arm with and without the effect of prescribed
69 deformation; Section 4 summarizes the scopes of this study and concludes with suggestions for further work.

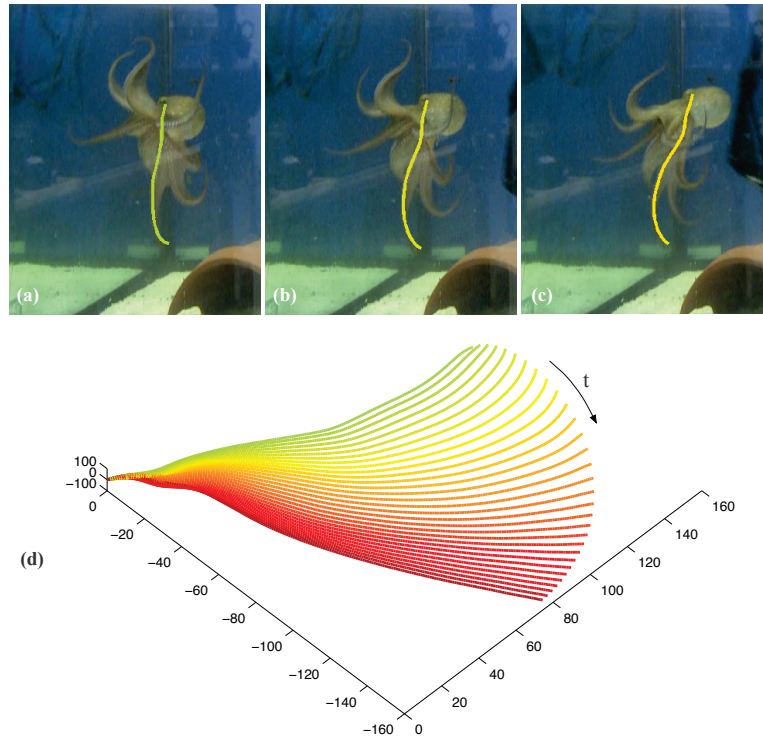


Figure 1: (a-c) Snapshots of octopus swimming in an aquarium [29]. The images are superimposed with segmented midlines of a single arm, color-coded according to the 3D arm reconstruction of (d), following the process described in the text. (d) The 3D arm trajectories are plotted here after translation of the starting point (here the eye of the octopus) to zero [30, 31, 32]; all dimensions are in millimetres. The plot concerns only the *power stroke* part (closing of the arms) of a more-complicated arm-swimming motion.

70 2. Methods

71 2.1. Octopus arm kinematics

72 Figures 1a-1c show snapshots of an octopus performing arm-swimming motion in an aquarium [29]. The images
 73 also depict the topological skeleton (midline) of a single arm, after being extracted automatically, for every snapshot,
 74 following the process described in detail in Yekutieli et al. [33]. Such 2D midlines can be extracted, similarly, from
 75 multiple cameras, synchronized to record the motion of live octopus. Using a set of three high-definition cameras and
 76 a checkerboard pattern for camera calibration [30, 31], the intrinsic and extrinsic camera parameters were estimated,
 77 according to a traditional grid based calibration technique [34]. This process allows for a robust calculation of the
 78 world Cartesian coordinates from the projective pinhole camera coordinates. By employing epipolar geometry con-

79 straints and least-square approximation, between each camera view, the 3D reconstruction of the medial axis of an
 80 individual arm was obtained for every video frame [31, 32]. Figure 1d displays the reconstructed 3D trajectories of
 81 the arm indicated in Figures 1a-1c; the trajectories are plotted after translation, such that their starting point (corre-
 82 sponding, here, to the eye of the octopus) is at zero position at all times. This allows identification of the arm motion
 83 separately from the motion of the animal’s body. The motion of the arm during swimming is evidently complex and,
 84 therefore, such motions are in general difficult to model. However, the motion can be simplified and be broadly char-
 85 acterized by a primary rotation around the starting position, and a deformation with time. Such approach is useful in
 86 capturing the fundamental characteristics of complex movements and was also used in this work.

87 2.2. Arm geometry and motion approximation

88 A first attempt to model realistic movements of individual cephalopod appendages, such as the reconstructed
 89 trajectories shown in Figure 1, is to consider simplified rotations of a slender octopus-like arm, around its fixed base.
 90 The arm was approximated with a right circular conical frustum, of a 9.75:1 taper ratio (length, L , to base-diameter,
 91 D) and a 17.5:1 aspect ratio (length to mean-diameter), for numerical simulations in quiescent fluid (Figures 2, 3). The
 92 temporal variation of the angular velocity $\omega(t)$ and the angle of rotation $\phi(t)$ may take various forms for a two-stroke
 93 motion profile, in which the arm rotates upwards and downwards in a cyclic way. Here, we examine two basic profiles,
 94 as displayed in Figures 2a, 2b: a sinusoidal oscillation, and a *sculling* profile [35, 36, 37, 38] of different velocity ratio
 95 β between a relatively slow upstroke (termed as *recovery stroke* [35]) and a considerably faster downstroke (termed
 96 *power stroke* [35]). These motion profiles originate from observations of live octopus and analysis of the reconstructed
 97 3D arm trajectories, during arm-swimming motion, in the way described in the previous paragraph and presented in
 98 Figure 1. The profiles can be formulated as follows:

$$Oscillation : \omega(t) = -A \sin(t), \quad 0 \leq t \leq T, \quad (1)$$

99

$$Sculling : \quad \omega(t) = \begin{cases} P_1(t), & 0 \leq t \leq t_1; \\ -\omega_r, & t_1 < t \leq T_r - t_1; \\ P_2(t - T_r), & T_r - t_1 < t \leq T_r + \beta t_1; \\ \omega_p, & T_r + \beta t_1 < t \leq T - \beta t_1; \\ P_3(t - T), & T - \beta t_1 < t \leq T, \end{cases} \quad (2)$$

100 where A is the amplitude of oscillation, ω_r is the angular velocity of the recovery stroke (upstroke), and $\omega_p = \beta\omega_r$
 101 is the angular velocity of the power stroke (downstroke). The times $t_1 = \frac{A}{18\omega_r}$ and $T_r = \frac{61A}{30\omega_r}$ are, respectively, those
 102 required by $\omega(t)$ to reach the value of $-\omega_r$, from zero, and the recovery stroke duration. The time $T_p = -\frac{3}{5\beta}(\beta^2 + 60)t_1$
 103 is the power stroke duration, and T is the total duration of the cyclic motion ($T = T_r + T_p$ for sculling). The functions
 104 P_1, P_2, P_3 are 4th degree polynomials, defined such that $\omega(t)$ is C^2 continuous at all times and the area integral over
 105 one period of the cyclic motion is zero, as follows:

$$\begin{aligned} P_1(t) &= -2\omega_r \frac{t}{t_1} + 2\omega_r \frac{t^3}{t_1^3} - \omega_r \frac{t^4}{t_1^4}, & 0 \leq t \leq t_1; \\ P_2(t - T_r) &= 2\omega_r \frac{t - T_r}{t_1} - 2\omega_r \frac{(t - T_r)^3}{t_1^3} - \omega_r \frac{(t - T_r)^4}{t_1^4}, & T_r - t_1 < t \leq T_r; \\ P_2(t - T_r) &= 2\omega_r \frac{t - T_r}{t_1} - 2\omega_r^3 \frac{(t - T_r)^3}{\omega_p^3 t_1^3} + \omega_r^4 \frac{(t - T_r)^4}{\omega_p^4 t_1^4}, & T_r < t \leq T_r + \beta t_1; \\ P_3(t - T) &= -2\omega_r \frac{t - T}{t_1} + 2\omega_r^3 \frac{(t - T)^3}{\omega_p^3 t_1^3} + \omega_r^4 \frac{(t - T)^4}{\omega_p^4 t_1^4}, & T - \beta t_1 < t \leq T. \end{aligned} \quad (3)$$

106 In addition to purely sinusoidal and sculling rotations of the arm, we investigate the effect of prescribed arm
 107 deformations [39, 40] in the form of traveling-wave undulations, which are in synchrony with the corresponding
 108 rotation frequencies (Figures 2c, 2d). The time-dependent deformation is imposed in a single direction (in the x -axis),
 109 that is, vertically to the longitudinal axis of the arm, according to the following function

$$d(z, t) = mz \sin(2\pi w z - 2\pi f_{\{r,p\}} t + 2\pi \chi_{\{r,p\}}), \quad (4)$$

110 where m is the scaled amplitude of the undulatory deformation and w is the number of wavelengths propagating along

111 the arm. For both the sinusoidal oscillation and sculling motions, the values of $m = 0.1$ and $w = 0.05$ were assumed.
 112 $f_{(r,p)}$ is the frequency of the traveling wave during the recovery and power strokes, respectively, and $\chi_{(r,p)}$ is the phase
 113 shift for the recovery and power strokes, respectively.

$$\text{For oscillation + undulation: } f_r = f_p = \frac{1}{T}, \quad \chi_r = \chi_p = 0. \quad (5)$$

$$\text{For sculling + undulation: } f_r = \frac{1}{2T_r}, f_p = \frac{1}{2T_p}, \quad \chi_r = \frac{T_r - 2T_p}{4T_r}, \chi_p = 0.25 - \frac{T_r}{2T_p}.$$

114 It is noted, that as a result of the unidirectional deformation, the arm elongates negligibly during the cyclic motion,
 115 and the tip acquires slightly sharper edges than when undeformed (Figures 2e, 2f).

116 All numerical solutions are initiated with an undeformed arm, at rest. A sigmoid function was applied to the defor-
 117 mation $d(z, t)$ only for the first few time steps of the 1st cycle, in order to create small increments of the deformation
 118 displacement and facilitate the simulation. The expression assumed for the sigmoid was as follows

$$S(t, a, b) = \frac{1}{1 + e^{-a(t-b)}}, \quad (6)$$

119 where a represents the growth rate and b sets the displacement of the sigmoid function along the arm's length. For
 120 both sinusoidal oscillation and sculling, the values of $a = 9$ and $b = 0.9$ were chosen. $S(t, a, b)$ was equal to 1 for
 121 $t > 0.25T$, during sinusoidal oscillation, and for $t > T_r$, during sculling.

122 Wake vortex topology in the simulations was visualized by the λ_2 criterion, as proposed by Jeong and Hussain
 123 (1995) [41], according to which, a vortex core is located at regions where the second eigenvalue λ_2 of the $S^2 + \Omega^2$ tensor
 124 is negative (S and Ω correspond, respectively, to the symmetric and antisymmetric parts of the velocity gradient). The
 125 helicity, H , was also used for the identification of the vortical structures. Helicity is a measure of the angle between
 126 the vectors of velocity, \mathbf{u} , and vorticity, $\boldsymbol{\omega} = \nabla \times \mathbf{u}$, defined as $H = \int \mathbf{u} \cdot \boldsymbol{\omega} dV$ [42] in volume V , and describes the
 127 topological linking and direction of rotation of vortex lines [43, 44].

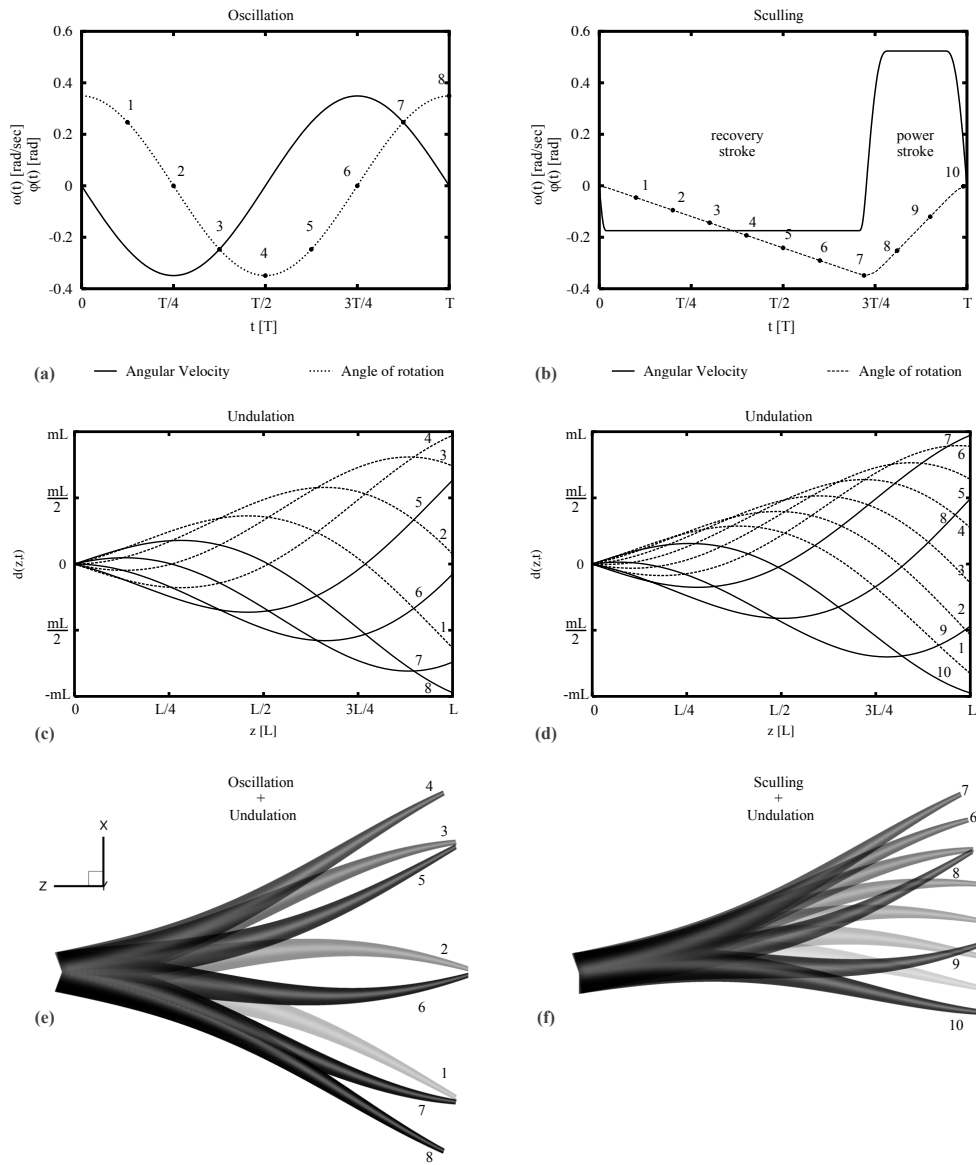


Figure 2: (a) Sinusoidal oscillation and (b) sculling motion profiles, displaying temporal variation of angular velocity and angle of rotation, for each case. (c-d) Time-dependent spatial deformation prescribed on the arm in the form of wavelike undulations that match up with the corresponding frequencies of oscillation and sculling. (e) Oscillatory rotation around the arm base combined with wavelike arm undulation of the same frequency ($A = 20^\circ$). (f) Sculling rotation around the arm base combined with arm undulation in synchronized sculling frequencies, using the profiles shown in (b) and (d) ($A = 10^\circ$). Numerals are distinguished in left and right columns: (a), (c), (e), and (b), (d), (f). (L is the arm length; m is the scaled amplitude, cf. Equation 4.)

128 2.3. Governing equations and numerical approaches

129 A Newtonian fluid was assumed, governed by the incompressible Navier-Stokes equations [45, 46], according to
 130 the following formulation

$$\frac{\partial \mathbf{u}}{\partial t} + (\mathbf{u} \cdot \nabla) \mathbf{u} = -\frac{1}{\rho} \nabla p + \nu \nabla^2 \mathbf{u}, \quad (7)$$

$$\nabla \cdot \mathbf{u} = 0, \quad (8)$$

131 where $\mathbf{u}=[u, v, w]$ is the velocity vector, ρ is the fluid density, p is the pressure, and ν is the kinematic viscosity. The
 132 Reynolds number, $Re_D = UD/\nu$, is a characteristic of the flow, where U is a velocity scale, and D is, here, the base
 133 diameter of the octopus-like arm. Typical values of the Reynolds number for motions of octopus arms in seawater are
 134 of the order of 1000 [47, 48]. This value ($Re_D = 1000$) was therefore adopted also in the current simulations, for a
 135 Reynolds number based on the arm base diameter [49, 14].

136 Two numerical approaches were used initially (Figures 3, 4) to determine the mesh requirements that must be
 137 employed for sufficiently capturing the boundary layer in the investigated forced motions: a finite volume (FV) and
 138 an immersed boundary (IB) approach. The rest of the computations (Figures 5 - 11) were performed with the IB
 139 approach.

140 *Finite Volume (FV) framework:* The FV numerical simulations were carried out with Fluent (ANSYS, Canons-
 141 burg, PA) by utilizing a second-order upwind discretization scheme for momentum, a second-order pressure dis-
 142 cretization scheme and the SIMPLE algorithm for pressure-velocity coupling. The ANSA (BETA CAE Systems S.A.,
 143 <http://www.beta-cae.gr>) mesh generation package was used to construct body-fitted prismatic elements at the near wall
 144 region of the arm within unstructured hybrid-type meshes. The spatial discretization around the arm was found more
 145 than sufficient to numerically capture the boundary layer growth and vortex generation during the arm movement, en-
 146 abling accurate evaluation of viscous flow effects. A volume mesh of 18.76×10^6 tetrahedral elements was constructed
 147 in a computational domain that was 46D in the x -direction, 31D in the y -direction and 20D in the z -direction; the
 148 arm base was located 15D away from the upstream and lateral edges of the domain. The entire mesh rotated as a
 149 solid body without deformation and a moving mesh strategy, available in the flow solver, was adopted, allowing the

150 high-resolution computational mesh to follow the arm at all instances of the cyclic movement. The quality and density
151 of the mesh in the near-wake field, guarantees high resolution of the near-wall region and good preservation of the
152 generated vortex patterns, with little diffusion, thus ensuring high fidelity and accuracy in our computations [14].

153 *Immersed Boundary (IB) framework:* The IB solution was computed using the curvilinear/immersed boundary
154 (CURVIB) method, described in detail in Gilmanov and Sotiropoulos (2005) [24] and Ge and Sotiropoulos (2007)
155 [25]. The code uses an immersed-boundary approach to solve the time-dependent, incompressible Navier-Stokes
156 equations in generalized curvilinear coordinates. The fluid domain is discretized with a background curvilinear fixed
157 grid, while the immersed body is treated as a sharp-interface boundary, discretized with an unstructured mesh. The
158 position of the immersed body is tracked and its motion is accounted for by reconstructing the solution at the IB
159 nodes in the immediate vicinity of the fluid/solid interface, using a quadratic interpolation (2nd order accurate) [24].
160 Nodes inside the solid immersed body (solid nodes) are blanked out and do not affect the solution on the fluid nodes.
161 Pressure-field boundary conditions at the IB nodes are not explicitly required because of the hybrid formulation of the
162 method [24]. Discretization in time is performed implicitly via a second-order accurate fractional step method for the
163 time integration of the governing equations.

164 The CURVIB method is coupled with the matrix-free Newton-Krylov solver, available in the PETSc library, for
165 the implicit solution of the momentum equations, and a very robust, multigrid-preconditioned GMRES solver, for the
166 solution of the pressure-correction equation [25]. The flow solver is parallelized using the MPI and PETSc libraries.
167 The background fluid mesh is parallelized by assigning a set of grid nodes to each processor using the PETSc's
168 modules, which also manage parallel communications for structured mesh problems. The walltime per one step of
169 the simulations with the CURVIB method (e.g. for those of Section 3.4), was 0.019 hrs, for a run of 800 steps per
170 one cycle. The CURVIB method has been extensively validated and applied to a range of problems [50], e.g. vortex-
171 induced vibrations; pulsatile, physiological, transitional flow in mechanical heart valves; aquatic swimming [12, 51];
172 turbulent flow in rivers with hydraulic structures; and flows past wind turbine rotors.

173 In this study, a 20 million structured cuboid grid was used for the fluid domain of the case solved with the
174 IB method. The grid extended 30D in both the x - and z -directions and 15D in the y -direction. A second, 1.5-
175 times smaller domain in the z -direction was constructed with 13 million structured elements to run the preliminary

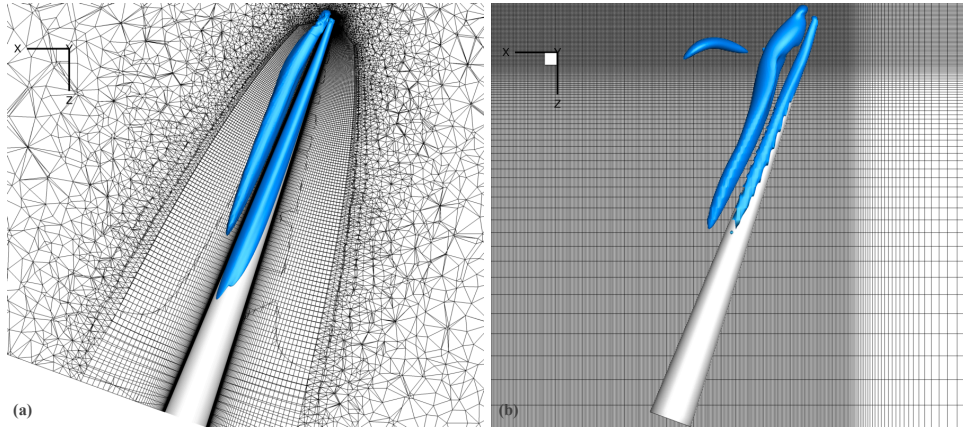


Figure 3: (a) Finite-volume solution, and (b) immersed-boundary solution of an octopus-like arm performing sinusoidal oscillation in the xz -plane. Instantaneous iso-contours of the λ_2 criterion [41] showing vortex topology ($\lambda_2 = -5$).

176 comparative studies of Figures 3a, 3b. In both grids, an inner region of size $8D \times D \times 2D$ was constructed with a
 177 uniform mesh, with an element spacing of $h = 0.02D$, to enclose the arm tip at all instances during the cyclic motions
 178 and to sufficiently capture the fine details of tip-initiated flow separation. The remaining grid was stretched towards
 179 this inner region with the use of a hyperbolic tangent stretching function. The aspect ratio of the largest corner element
 180 was 1.56.

181 The total hydrodynamic force, F , acting on the moving arm can be decomposed into the three Cartesian compo-
 182 nents (F_x, F_y, F_z), along the x , y and z directions of the computational domain. The hydrodynamic force coefficients
 183 ($C_{F_x}, C_{F_y}, C_{F_z}$) are defined as follows:

$$C_{F_i} = \frac{F_i}{\frac{1}{2}\rho U^2 A} \quad (9)$$

184 where $i = \{x, y, z\}$ and A is the reference area, here taken as the projected frontal area of the undeformed arm.

185 3. Results

186 3.1. Results of sinusoidal oscillation of the arm

187 A solid-body sinusoidal oscillation was examined first with both the FV and IB numerical approaches, to verify
 188 the mesh requirements for sufficiently capturing the boundary layer growth around the arm. The arm rotated around

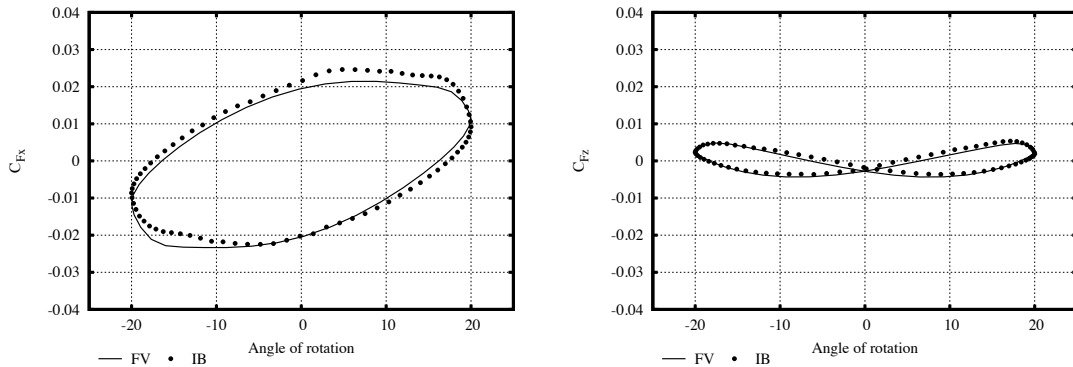


Figure 4: Comparison of the hydrodynamic force coefficients calculated by two numerical approaches, for an arm performing sinusoidal oscillation in the xz -plane. The solid line is evaluated by the Finite Volume (FV) method, whereas the dotted line by the Immersed Boundary (IB) method.

189 its base with a time-varying angular velocity $\omega(t)$ according to Equation 1, with $A = 20^\circ$ (figure 3). Although small in
 190 magnitude, the motion resulted in two counter-rotating vortices on the trailing sides of the arm, for each stroke. Figure
 191 3 shows vortex topology at the end of the second cycle, visualized as instantaneous iso-contours of the λ_2 criterion
 192 (according to Jeong and Hussain, 1995 [41]). The result of Figure 3a is calculated by the finite-volume method, as
 193 described in Section 2.3, and that of Figure 3b, by the immersed-boundary method, on the somewhat coarser mesh
 194 (13 million elements, cf. Section 2.3). In the FV case, the computational mesh rotated together with the arm, whereas,
 195 in the IB case, the background grid was fixed. The presence of two counter-rotating vortices originating from the tip
 196 and extending along the lee side of the arm, at a close distance from the wall, up to about half the arm length, was
 197 confirmed in both solutions.

198 The C_{F_x} and C_{F_z} force coefficients are displayed in Figures 4a, 4b, respectively, as a function of the angle of
 199 rotation. Time-periodicity was achieved after about 2 periods. The results show that the force components varied
 200 with the angle of rotation: for C_{F_z} , the motion produced positive thrust during upstroke and negative thrust during
 201 downstroke, resulting in an effectively almost zero forward thrust in the positive z -direction (integral of the C_{F_z} curve
 202 with respect to the angle of rotation for one complete period). The solutions obtained from both the finite-volume and
 203 the immersed-boundary approaches are in good agreement.

204 Figures 5a, 5c display instantaneous vortex structures, as obtained with the IB approach, from later times of the

205 cyclic motion at maximum amplitudes, using the finer grid (20 million elements, cf. Section 2.3). During most of this
206 solid-body sinusoidal oscillation, the angular frequency is small, reaching maximum values only for a few instances.
207 In addition, the amplitude and time duration of the motion are relatively large, allowing the vortices to diffuse between
208 recurrent upstrokes and downstrokes of the arm. Nevertheless, few seemingly non-canonical vortical structures appear
209 in the wake of the arm for both time instances presented.

210 3.2. Results of sinusoidal arm oscillation combined with arm undulation

211 The sinusoidal rotation of the arm (motion profile of Figure 2a) was subsequently combined with a wavelike
212 arm undulation, according to Equation 4 and the parameters described in Section 2.2. The time-dependent spatial
213 deformation along the arm's length is illustrated individually in Figure 2c, in which the dashed lines correspond to the
214 upstroke (numerals from 1 to 4) and the solid lines to the downstroke (numerals from 5 to 8). The arm undulation is
215 adjusted to be in synchrony with the sinusoidal rotation of the arm; therefore, the arm acquires maximum deformation
216 at the maximum angle of rotation. As Figure 2e shows, incorporation of the undulation to the sinusoidal rotation,
217 produces considerable deformation to the arm during the cyclic motion. The figure shows the deformed arm at
218 instances where the activation function $d(z, t)$ is in full effect along the entire arm. Arm positions colored with light
219 gray correspond to the upstroke (numerals 1 to 4), whereas darker-colored positions correspond to the downstroke
220 (numerals 5 to 8). These positions can be tracked also in Figures 2a and 2c at the respective instances.

221 Figures 5b and 5d show vortex topology at positions of maximum arm deformation (and rotation). (It is noted that
222 the xz -plane is slightly rotated for better visualization of the vortical structures near the tip.) Two counter-rotating
223 vortices appear again in the lee side of the arm with respect to the direction of motion (upstroke and downstroke),
224 although they are deformed, following the deformation of the arm wall. These figures also display an increased
225 separation of flow from the tip, as compared to the undeformed arm at the same time instances (Figures 5a, 5c).
226 There appears to be greater flow disturbance in the region near the tip's leeward side, shedding an extended street
227 of non-canonical vortices in the wake, of opposite helicity. The increase in the flow separation from the tip may
228 admittedly be enhanced by the unidirectional deformation that slightly distorts the tip. Nevertheless, the deformation
229 itself increases the angle of attack for a bigger section of the arm near the tip, encouraging the disturbance of flow
230 during both upstroke and downstroke.

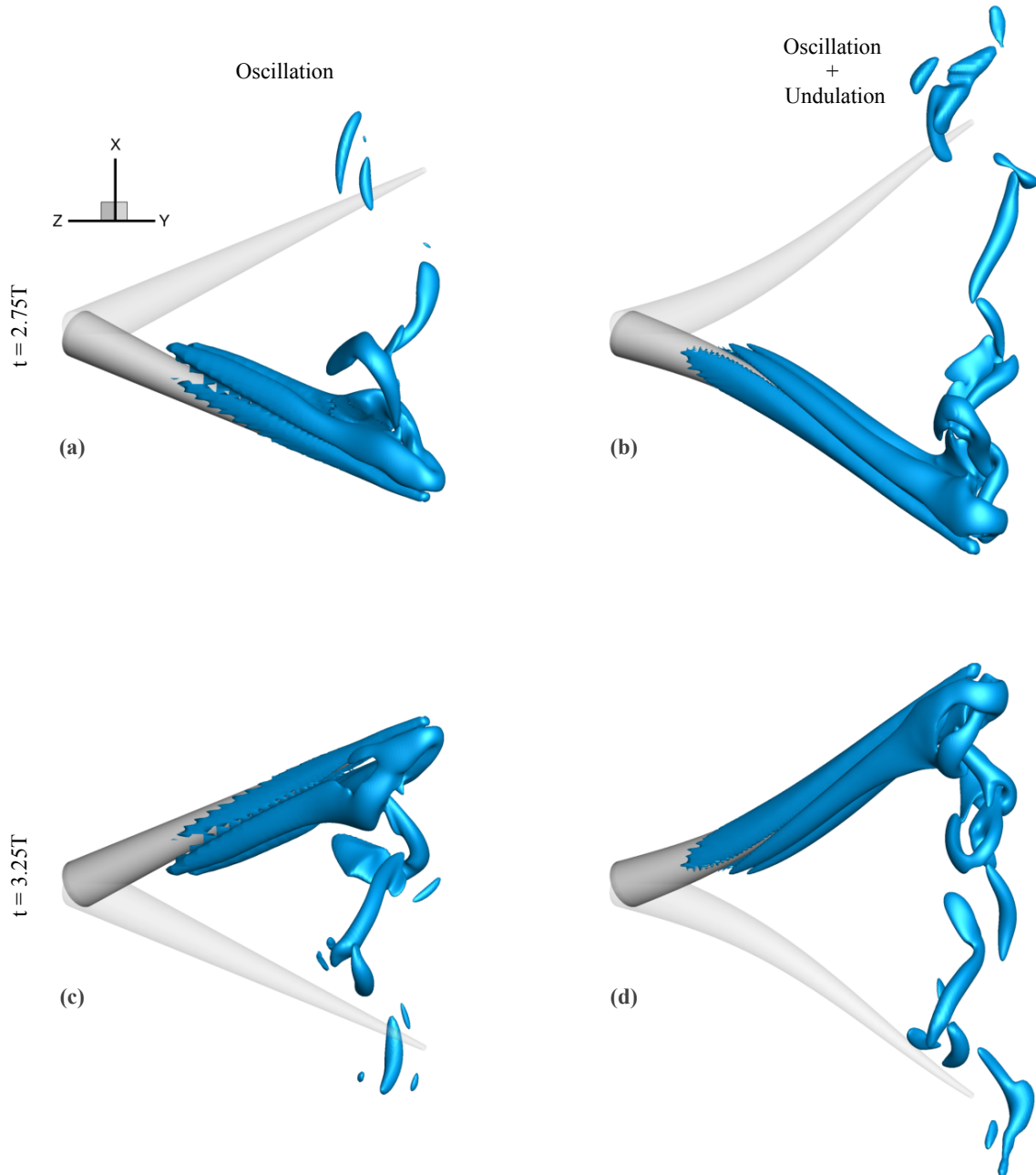


Figure 5: Instantaneous near-wake vortex patterns for sinusoidal oscillation around the arm base (a, c) without and (b, d) with arm undulations, obtained with the IB approach. Instances are shown at positions of maximum amplitude (a-b) $t = 2.75T$ and (c-d) $t = 3.25T$ ($\lambda_2 = -1$). Positions at the opposite maximum amplitude are also depicted with light color, to indicate the direction of movement and the angular span. Note that the xz -plane is rotated for a better visualization of the vortical structures.

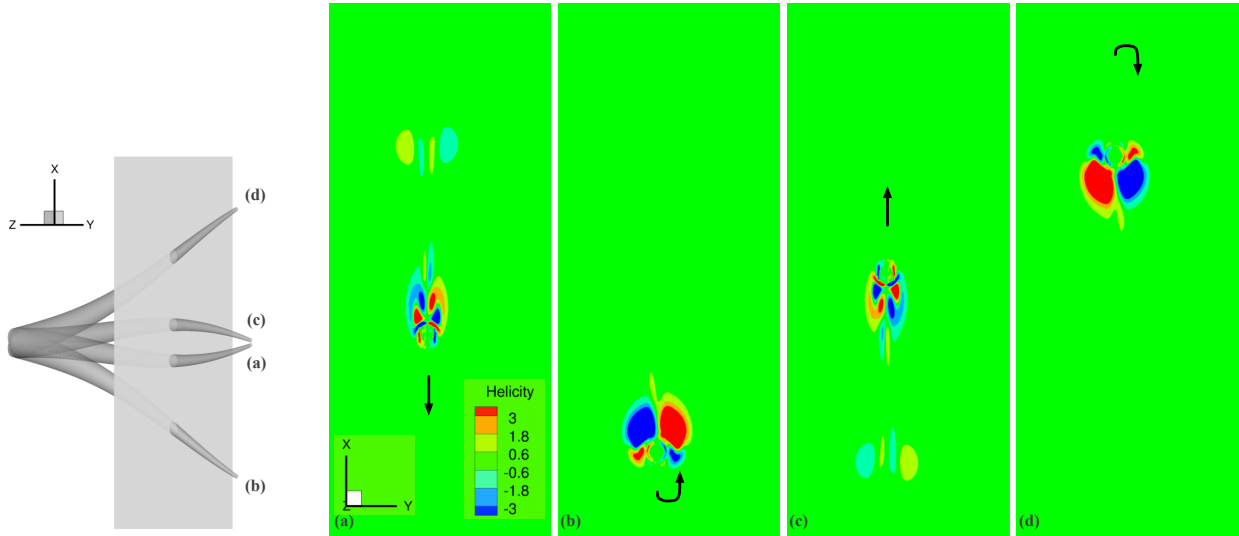


Figure 6: Evolution of vortical structures visualized according to helicity, on a fixed plane near the middle of the arm, at a distance $0.67L$ from the arm base, for sinusoidal oscillation combined with arm undulation. (Left) Positions of the arm with respect to the plane. (Right) Helicity contours at $t =$ (a) $1.35T$ (middle of upstroke, recovery), (b) $1.725T$ (end of upstroke, recovery), (c) $1.85T$ (middle of downstroke, power), (d) $2T$ (end of downstroke, power). Instances in (b) and (d) correspond to instances shown in Figures 5b and 5d, respectively. Arrows show direction of movement.

231 Figures 6 and 7 display the evolution of vortical structures visualized according to helicity, on fixed planes near
 232 the middle of the arm, at a distance $0.67L$ from the arm base, and the tip of the arm, at a distance $0.93L$ from the
 233 arm base, respectively. There is considerable flow separation from the arm tip throughout the cyclic motion. Near the
 234 middle of the arm, the evolution of the flow is different. The well-formed counter-rotating vortices appear to be the
 235 main contributors to the generated thrust. These results are in consistent with the λ_2 vortex topology of Figures 5b
 236 and 5d.

237 3.3. Results of arm sculling

238 A second cyclic motion was investigated, termed as *sculling* [52, 35, 36, 37], by adopting the motion profile of
 239 Figure 2b. According to Equation 2 and the parameters described in Section 2.2, the motion is composed of a slow
 240 recovery (upstroke) and fast power (downstroke). Here, the following values were assumed: $A = 10^\circ$ $\omega_r = 10^\circ/sec$
 241 and $\beta = 3$. This motion profile was prescribed by a set of polynomial expressions P_1, P_2, P_3 , according to Equations
 242 2 and 3, to allow C^2 continuous transitions between the constant values of ω_r and $\beta\omega_r$ of the sculling. The solid-body

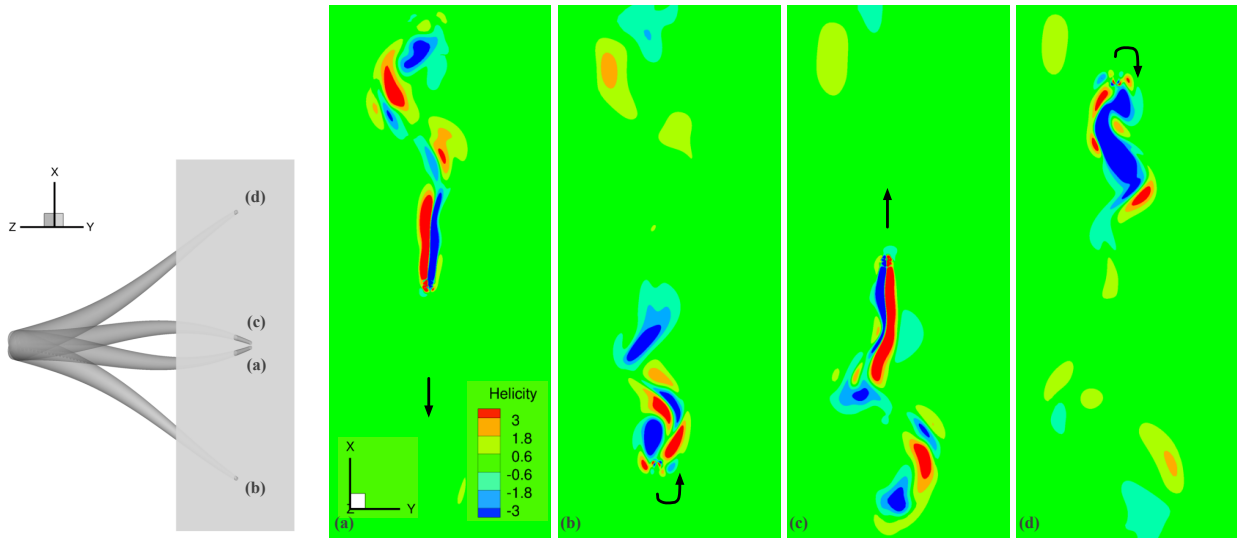


Figure 7: Evolution of vortical structures visualized according to helicity, on a fixed plane near the tip of the arm, at a distance $0.93L$ from the arm base, for sinusoidal oscillation combined with arm undulation. (Left) Positions of the arm with respect to the plane. (Right) Helicity contours at $t =$ (a) $1.35T$ (middle of upstroke, recovery), (b) $1.725T$ (end of upstroke, recovery), (c) $1.85T$ (middle of downstroke, power), (d) $2T$ (end of downstroke, power). Instances in (b) and (d) correspond to instances shown in Figures 5b and 5d, respectively. Arrows show direction of movement.

243 motion examined here involves a smaller angular span than the sinusoidal oscillation described earlier.

244 Figure 8a depicts instantaneous vortical patterns as observed at the end of the recovery stroke (at $t = 1.725T$) and
 245 Figure 8c at the end of the power stroke (at $t=2T$). Much like in the sinusoidal oscillation, the two counter-rotating
 246 vortices at the lee side of the arm are formed during this motion too; however, they appear thinner and somewhat more
 247 detached from the arm's wall. The angular frequency has considerably large values for the duration of the sculling
 248 movement, taking the value of ω_r for the most part of the cycle and then reaching the maximum value of $\beta\omega_r$ for
 249 almost one quarter of the cycle. In addition, the amplitude and time duration of the overall motion are relatively small
 250 (high f_r and f_p frequencies). Therefore, vortical structures generated in previous cycles do not diffuse in time for the
 251 subsequent upstroke and downstroke, and they continue to be visible in the flow field (vortical structures seen below
 252 the arm). The speed of the motion appears to result in abrupt separation from the tip, with very little shedding in the
 253 wake (as compared to the non-canonical vortices being shed during the slow sinusoidal oscillation, cf. Paragraph 3.1).

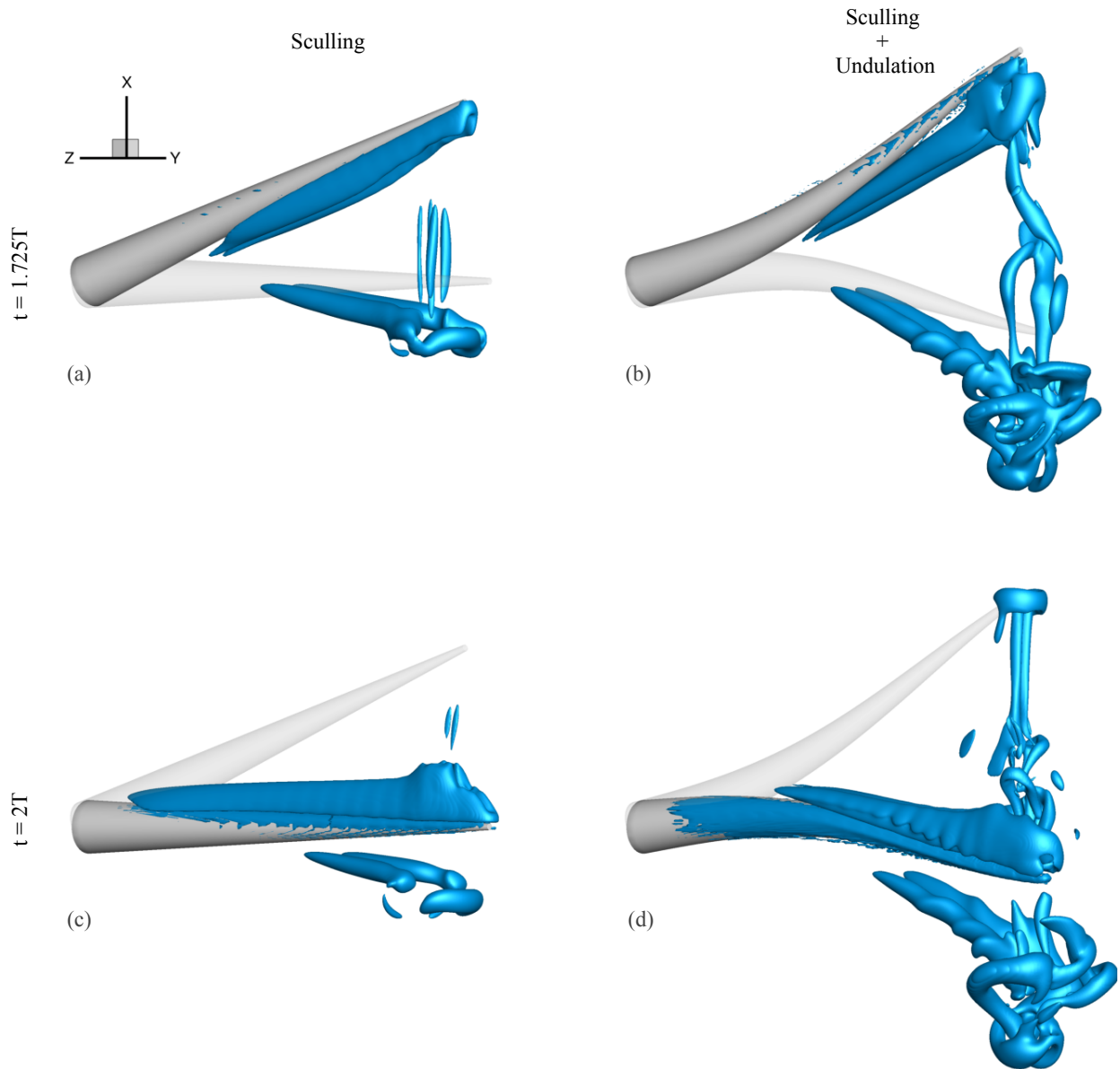


Figure 8: Instantaneous near-wake vortex patterns for sculling rotation around the arm base (a, c) without and (b, d) with arm undulations, obtained with the IB approach. Instances are shown at positions of maximum amplitude (a-b) $t = 1.725$ and (c-d) $t = 2T$ ($\lambda_2 = -1$). Positions at the opposite maximum amplitude are also depicted with light color, to indicate the direction of movement and the angular span. Note that the xz -plane is rotated for better visualization of the vortical structures.

254 3.4. Results of arm sculling combined with arm undulation

255 The sculling rotation of the arm (motion profile of Figure 2b) was combined with a wavelike arm undulation,
 256 according to Equation 4 and the parameters described in Section 2.2. The time-dependent spatial deformation along

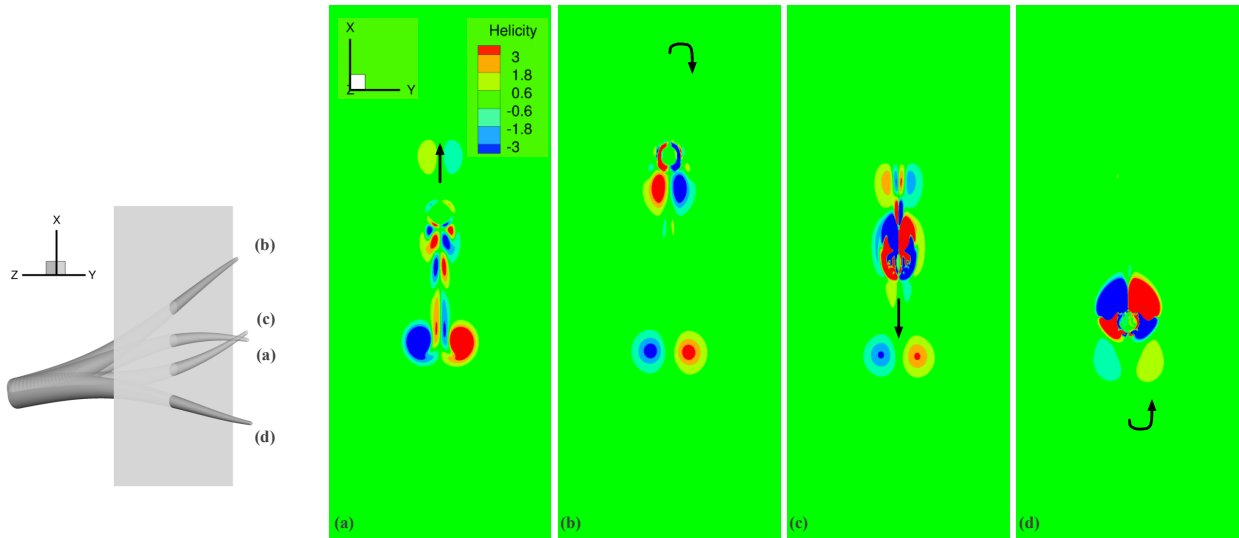


Figure 9: Evolution of vortical structures visualized according to helicity, on a fixed plane near the middle of the arm, at a distance $0.67L$ from the arm base, for sculling combined with arm undulation. (Left) Positions of the arm with respect to the plane. (Right) Helicity contours at $t =$ (a) $2.5T$ (middle of downstroke), (b) $2.75T$ (end of downstroke), (c) $3T$ (middle of upstroke), (d) $3.25T$ (end of upstroke). Instances in (b) and (d) correspond to instances shown in Figures 8b and 8d, respectively. Arrows show direction of movement.

257 the arm's length is illustrated individually in Figure 2d, in which the dashed lines correspond to the recovery stroke
 258 (upstroke, numerals from 1 to 7) and the solid lines to the power stroke (downstroke, numerals from 8 to 10). The fre-
 259 quencies of the arm undulation during recovery and power strokes are tuned to match up with the sculling frequencies
 260 (f_r and f_p , respectively), so that maximum arm deformation is acquired at the end of each stroke. Figure 2f illustrates
 261 the deformation to the arm during the sculling motion. The figure shows the deformed arm at instances where the
 262 activation function $d(z, t)$ is in full effect along the entire arm. Arm positions colored with light gray correspond to
 263 the recovery stroke (numerals 1 to 7), whereas darker-colored positions correspond to the power stroke (numerals 8 to
 264 10). These positions can be tracked also in Figures 2b and 2d at the respective instances.

265 Figures 8b and 8d show vortex topology at positions of maximum arm deformation. (Note again that the xz -plane
 266 is slightly rotated for better visualization of the vortical structures near the tip.) Compared to the results of Figures 5b,
 267 5d, the two counter-rotating vortices in the leeward side of the arm, with respect to the direction of motion (recovery
 268 and power strokes), appear to follow only loosely the deformation of the arm wall, and are more detached near the

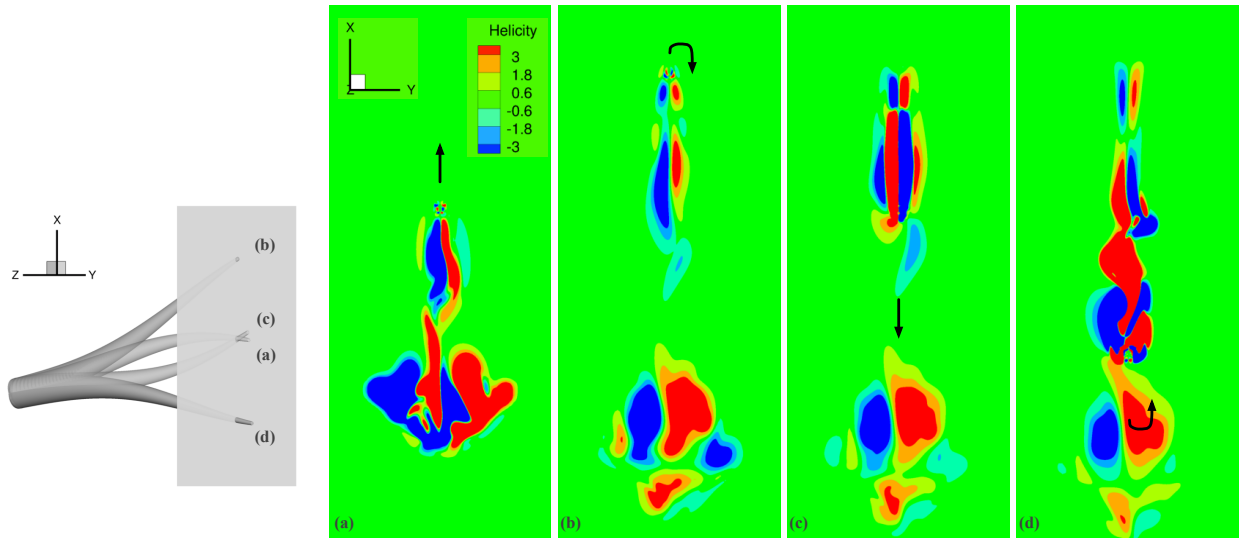


Figure 10: Evolution of vortical structures visualized according to helicity, on a fixed plane near the tip of the arm, at a distance $0.93L$ from the arm base, for sculling combined with arm undulation. (Left) Positions of the arm with respect to the plane. (Right) Helicity contours at $t =$ (a) $2.5T$ (middle of downstroke), (b) $2.75T$ (end of downstroke), (c) $3T$ (middle of upstroke), (d) $3.25T$ (end of upstroke). Instances in (b) and (d) correspond to instances shown in Figures 8b and 8d, respectively. Arrows show direction of movement.

269 tip. There is also increased separation of the flow from the tip and greater disturbance in the wake, in comparison
 270 to the undeformed arm at the same time instances (left column of Figures 8). Complex vortical structures generated
 271 in previous cycles do not appear to diffuse in time for the subsequent upstroke and downstroke. These structures are
 272 clearly visible in the time instances displayed in Figure 8 (right column): during the upward movement of the arm
 273 (Figure 8b), a small part of the large disturbed-flow structure generated in the previous cycle is drifted, while shedding
 274 new structures in the wake; during the the rapid downward return of the arm (like flapping, Figure 8d), the previous
 275 disturbed-flow structure is pushed further downwards.

276 Figures 9 and 10 display the evolution of vortical structures visualized according to helicity, on fixed planes near
 277 the middle of the arm, at a distance $0.67L$ from the arm base, and the tip of the arm, at a distance $0.93L$ from the arm
 278 base, respectively. There is extensive flow separation from the arm tip throughout the cyclic motion. Near the middle
 279 of the arm, however, the flow disturbance is different from that of the tip. The well-formed counter-rotating vortices
 280 seen at this region are the main generators of thrust. These results are in consistent with the λ_2 vortex topology of

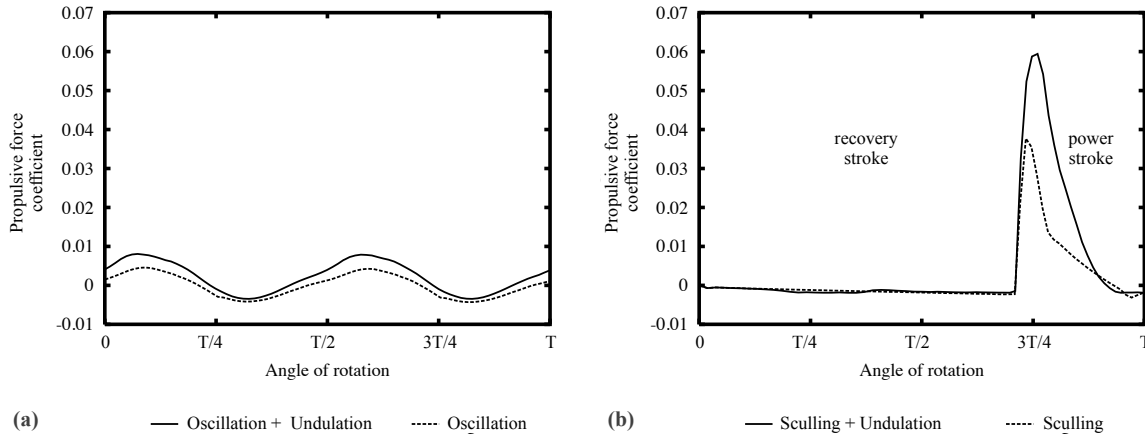


Figure 11: Temporal variation of the propulsive force coefficient, resulting from (a) oscillation and (b) sculling of the arm around its base, either alone or combined with arm undulations. Results obtained with the IB approach.

281 Figures 8b and 8d.

282 4. Discussion and conclusions

283 The hydrodynamic propulsive force coefficients generated in the direction of positive z (that is, towards the arm
 284 base) are shown for all four cases presented, in Figure 11. Calculated forces for pure sinusoidal oscillation and sculling
 285 are displayed with dashed lines, whereas those for rotations combined with undulations are depicted with solid lines,
 286 in both Figures 11a and 11b. The effect of arm undulation on the generated propulsive force is evident for both the
 287 sinusoidal oscillation and sculling. In sinusoidal oscillation, the increase is almost uniform, resulting in the generation
 288 of a small forward thrust (Figures 11a). In sculling, the effect is larger, particularly during the power stroke (Figures
 289 11b), producing a considerably larger forward thrust.

290 Incorporation of arm deformation appears, thus, to increase the output thrust of the combined system. Indeed, a
 291 single arm rotating as a solid body around its base is a single-degree-of-freedom system, with a single joint at its base.
 292 This system adds some energy to the surrounding flow field in the form of the vortical structures seen in Figures 5a,
 293 5c and 8a, 8c. The prescribed wavelike undulations of the arm, however, increase drastically the number of degrees-
 294 of-freedom of the system, since every finite element on the arm's surface can be thought to act as a finite joint, adding
 295 extra energy to the flow field (Figures 5b, 5d and 8b, 8d); and, hence, producing extra thrust. This case differs from

296 a compliant arm that would deform as a result of its interaction with the flow, and would require a fluid-structure
297 interaction numerical approach to investigate.

298 We are interested specifically in the prescribed activation of the arm, that would be based on realistic octopus
299 arm kinematics (such as that of Figure 1), since octopus appendages are known to actively take part in many of the
300 observed behaviors (e.g., arm-swimming, head-up swimming, crawling, etc.). Admittedly, these movements are far
301 more complex than the simplified motion profiles we considered here. We used the immersed boundary approach in
302 order to simulate the deformation of an arm during these simplified movements and better understand the unsteady
303 hydrodynamics of the mechanism, since the extremely large deformations of the mesh required with body-fitted
304 finite-element or finite-volume approaches, are very hard to achieve even with the most advanced mesh deformation
305 techniques. It was found that the sculling motion combined with arm undulation is an effective propulsive scheme for
306 an octopus-like arm. One direction towards simulating more realistic locomotion patterns is to include translation of
307 the arm as a result of the generated propulsive force. This aspect, combined with a more accurate definition of the
308 deformation on the arm, may provide a deeper insight underlying cephalopod-like propulsive systems. Furthermore,
309 the inclusion of a second or more arms may help analyze possible interaction among different arms.

310 Aiming at a computation tool able to model intense motions, as found in aquatic locomotion instances, two
311 numerical methods were compared initially. The immersed boundary method demonstrates its suitability for handling
312 such motions. We aim to further adjust this method for special flow characteristics of time-varying geometries under
313 more complex prescribed motions.

314 **Acknowledgments**

315 This work was supported in part by the European Commission (EC) and the General Secretariat for Research and
316 Technology (GSRT) of the Hellenic Ministry of Education via the ESF-GSRT HYDRO-ROB Project [PE7(281)] and
317 the EC-ERDF BIOSYS-KRIPIS Project [MIS-448301 (2013SE01380036)]. Parts of these simulations were carried
318 out on the CaSToRC High-Performance Computing (HPC) system, of the LINKSCEEM/Cy-Tera resources (Project
319 pro14a108) and the PRACE Tier-1 HPC system (Project CepFlow, 12DECI0048). The authors would like to thank
320 B. Hochner, T. Flash, M. Sfakiotakis, X. Zabulis, M. Kuba, J. Oikonomidis, A. Chatzidaki, Th. Evdaimon, and S.

321 Stefanou, for their assistance with these studies.

322 References

- 323 [1] W.M. Kier, K.K. Smith, Tongues, tentacles and trunks: the biomechanics of movement in muscular-hydrostats, *Zool J Linn Soc* 83 (1985)
324 307–324.
- 325 [2] C.L. Huffard, Locomotion by *Abdopus aculeatus* (Cephalopoda: Octopodidae): Walking the line between primary and secondary defenses, *J*
326 *Exp Biol* 209 (2006) 3697–3707.
- 327 [3] E.J. Anderson, M.E. Demont, The mechanics of locomotion in the squid *Loligo pealei*: locomotory function and unsteady hydrodynamics of
328 the jet and intramantle pressure, *J Exp Biol* 203 (2000) 2851–2863.
- 329 [4] M. Sfakiotakis, D.M. Lane, J.B.C. Davies, Review of fish swimming modes for aquatic locomotion, *IEEE J Ocean Eng* 24 (2) (1999) 237–252.
- 330 [5] G.V. Lauder, E.G. Drucker, Forces, fishes, and fluids: Hydrodynamic mechanisms of aquatic locomotion, *Physiology* 17 (2002) 235–240.
- 331 [6] J.C. Liao, D.N. Beal, G.V. Lauder, M.S. Triantafyllou, Fish exploiting vortices decrease muscle activity, *Science* 302 (2003) 1566–1569.
- 332 [7] J.C. Liao, D.N. Beal, G.V. Lauder, M.S. Triantafyllou, The *kármán* gait: novel body kinematics of rainbow trout swimming in a vortex street,
333 *J Exp Biol* 206 (2003) 1059–1073.
- 334 [8] E.D. Tytell, G.V. Lauder, The hydrodynamics of eel swimming. i. wake structure, *J Exp Biol* 207 (2004) 1825–1841.
- 335 [9] E.D. Tytell, The hydrodynamics of eel swimming. ii. effect of swimming speed, *J Exp Biol* 207 (2004) 3265–3279.
- 336 [10] J.O. Dabiri, S.P. Colin, J.H. Costello, Fast-swimming hydromedusae exploit velar kinematics to form an optimal vortex wake, *J Exp Biol* 209
337 (2006) 2025–2033.
- 338 [11] I.K. Bartol, P.S. Krueger, J.T. Thompson, W.J. Stewart, Swimming dynamics and propulsive efficiency of squids throughout ontogeny, *Integr*
339 *Comp Biol* 48 (6) (2008) 720–733.
- 340 [12] I. Borazjani, F. Sotiropoulos, Numerical investigation of the hydrodynamics of carangiform swimming in the transitional and inertial flow
341 regimes, *J Exp Biol* 211 (2008) 1541–1558.
- 342 [13] G.V. Lauder, *Animal locomotion*, Heidelberg, Germany, Springer-Verlag, 2010, Ch. Swimming hydrodynamics: Ten questions and the
343 technical approaches needed to resolve them, pp. 3–15.
- 344 [14] A. Kazakidi, V. Vavourakis, D. P. Tsakiris, J. Ekaterinaris, A numerical investigation of flow around octopus-like arms: near-wake vortex
345 patterns and force development, *Comp. Meth. Biomech. Biomed. Eng.* 18 (12) (2015) 1321–1339.
- 346 [15] P.D. Thomas, C.K. Lombard, Geometric conservation law and its application to flow computations on moving grids, *AIAA Journal* 17 (10)
347 (1979) 1030–1037.
- 348 [16] I. Demirdzic, M. Peric, Space conservation law in finite volume calculations of fluid flow, *Int. J. Numer. Meth. Fluids* 8 (1988) 1037–1050.
- 349 [17] C. Peskin, Flow pattern around heart valves: a numerical method, *J Comput Phys* 10 (1972) 252–271.
- 350 [18] C. Peskin, D. McQueen, Shared-memory parallel vector implementation of the immersed boundary method for the computation of blood flow
351 in the beating mammalian heart, *J. Supercomput.* 11 (1997) 213–236.

- 352 [19] D. Goldstein, R. Handler, L. Sirovich, Modeling a no-slip flow boundary with an external force field, *J. Comput. Phys.* 105 (1993) 354–366.
- 353 [20] R. Cortez, M. Minion, The blob projection method for immersed boundary problems, *J. Comput. Phys.* 161 (2000) 428–453.
- 354 [21] R. LeVeque, Z. Li, Immersed interface method for stokes flow with elastic boundaries or surface tension, *SIAM J. Sci. Comput.* 18 (1997)
355 709–735.
- 356 [22] J. Mohd-Yusof, Combined immersed boundaries/b-splines methods for simulations of flows in complex geometries. center for turbulence
357 research., Annual Research Briefs, Stanford University, NASA Ames (1997) 317–327.
- 358 [23] E. Fadlun, R. Verzicco, P. Orlandi, J. Mohd-Yusof, Combined immersed-boundary finite-difference methods for three-dimensional complex
359 flow simulations., *J. Comput. Phys.* 161 (2000) 35–60.
- 360 [24] A. Gilmanov, F. Sotiropoulos, A hybrid cartesian/immersed boundary method for simulating flows with 3d, geometrically complex, moving
361 bodies, *J. Comp. Phys.* 207 (2005) 457–492.
- 362 [25] L. Ge, F. Sotiropoulos, A numerical method for solving the 3d unsteady incompressible navier–stokes equations in curvilinear domains with
363 complex immersed boundaries, *J Comput Phys* 225 (2007) 1782–1809.
- 364 [26] A. Kazakidi, D.P. Tsakiris, F. Sotiropoulos, J.A. Ekaterinaris, Numerical investigation of aquatic locomotion with cephalopod-like ap-
365 pendages, in: 19th Congr Europ Soc Biomech, (ESB2013), Patra, Greece, 2013.
- 366 [27] A. Kazakidi, D. P. Tsakiris, F. Sotiropoulos, J. A. Ekaterinaris, A computational fluid dynamic study of intense cephalopod-like motions, in:
367 44th AIAA Fluid Dynamics Conference, AIAA AVIATION, Atlanta, GA, USA, 2014.
- 368 [28] T.-H. Wu, R.-S. Guo, G.-W. He, Y.-M. Liu, D. Qi, Simulation of swimming of a flexible filament using the generalized lattice-spring lattice-
369 Boltzmann method, *J Exp Biol* 349 (2014) 1–11.
- 370 [29] A. Kazakidi, M. Kuba, A. Botvinnik, M. Sfakiotakis, T. Gutnick, S. Hanassy, G. Levy, J. A. Ekaterinaris, T. Flash, B. Hochner, D. P. Tsakiris,
371 Swimming patterns of the *Octopus vulgaris*, in: 22nd Annual Meeting NCM Society, Venice, Italy, 2012.
- 372 [30] A. Kazakidi, S. Stefanou, X. Zabulis, M. Kuba, A. Botvinnik, S. Hanassy, M. Sfakiotakis, T. Gutnick, J. A. Ekaterinaris, T. Flash, B. Hochner,
373 D. P. Tsakiris, Motion reconstruction of arm swimming in the *Octopus vulgaris*, in: 19th Congress of the European Society of Bioengineering
374 (ESB), Patra, Greece, 2013.
- 375 [31] A. Kazakidi, S. Stefanou, X. Zabulis, M. Kuba, J. A. Ekaterinaris, T. Flash, B. Hochner, D. P. Tsakiris, 3d reconstruction of octopus arm
376 swimming motion, in: 7th World Congress of Biomechanics (WCB), Boston, MA, USA, 2014.
- 377 [32] A. Kazakidi, X. Zabulis, D. P. Tsakiris, Vision-based 3d motion reconstruction of octopus arm swimming and comparison with an 8-arm
378 underwater robot, in: IEEE Int. Conf. Rob. Autom. (ICRA'15), Seattle, WA, USA, 2015 *in press*.
- 379 [33] Y. Yekutieli, R. Mitelman, B. Hochner, T. Flash, Analyzing octopus movements using three-dimensional reconstruction, *J. Neurophysiol.* 98
380 (2007) 1775–1790.
- 381 [34] R. Y. Tsai, A versatile camera calibration technique for high-accuracy 3d machine vision metrology using off-the-shelf TV cameras and
382 lenses, *IEEE Journal of Robotics and Automation* 3 (4) (1987) 323–344.
- 383 [35] M. Sfakiotakis, A. Kazakidi, N. Pateromichelakis, D.P. Tsakiris, Octopus-inspired eight-arm robotic swimming by sculling movements, in:
384 IEEE Int Conf Rob Autom, (ICRA 2013), Karlsruhe, Germany, 2013, pp. 5135–5141.

- 385 [36] M. Sfakiotakis, A. Kazakidi, D.P. Tsakiris, Turning maneuvers of an octopus-inspired multi-arm robotic swimmer, in: 21st Med Conf Control
386 Autom, (MED'13), Chania, Greece, 2013, pp. 1343–1349.
- 387 [37] M. Sfakiotakis, A. Kazakidi, A. Chatzidaki, T. Evdaimon, D. P. Tsakiris, Multi-arm robotic swimming with octopus-inspired compliant web,
388 in: IEEE/RSJ Int. Conf. on Int. Rob. Syst. (IROS'14), Chicago, Illinois, USA, 2014, pp. 302–308.
- 389 [38] M. Sfakiotakis, A. Kazakidi, D. P. Tsakiris, Octopus-inspired multi-arm robotic swimming, *Bioinspir. Biomim.* (2015) *in press*.
- 390 [39] V. Vavourakis, D. Bampasakis, A. Kazakidi, N. Pateromichelakis, J.A. Ekaterinaris, D.P. Tsakiris, Generation of primitive behaviors for
391 non-linear hyperelastic octopus-inspired robotic arm, in: IEEE Int Conf Biomed Robotics Biomechatron, (BioRob) Roma, Italy, 2012, pp.
392 725–730.
- 393 [40] V. Vavourakis, A. Kazakidi, D.P. Tsakiris, J.A. Ekaterinaris, A nonlinear dynamic finite element approach for simulating muscular hydrostats,
394 *Comput Methods Biomech Biomed Engin* 17 (8) (2014) 917–931.
- 395 [41] J. Jeong, F. Hussain, On the identification of a vortex, *J Fluid Mech* 285 (1995) 69–94.
- 396 [42] H. Moffatt, A. Tsinober, Helicity in laminar and turbulent flow, *Ann Review Fluid Mech* 24 (1992) 281–312.
- 397 [43] D. Degani, A. Seginer, Y. Levy, Graphical visualization of vortical flows by means of helicity, *AIAA Journal* 28 (8) (1990) 1347–1352.
- 398 [44] A. Pobitzer, R. Peikert, R. Fuchs, B. Schindler, A. Kuhn, H. Theisel, K. Matkovic, H. Hauser, The state of the art in topology-based
399 visualization of unsteady flow, *Computer Graphics Forum* 30 (6) (2011) 1789–1811.
- 400 [45] G.K. Batchelor, *An introduction to fluid dynamics*, Cambridge University Press, 2000.
- 401 [46] D.J. Tritton, *Physical fluid dynamics*, Oxford University Press, 1988.
- 402 [47] Y. Gutfreund, T. Flash, Y. Yarom, G. Fiorito, I. Segev, B. Hochner, Organization of octopus arm movements: A model system for studying
403 the control of flexible arms, *J Neurosci* 16 (1996) 7297–7307.
- 404 [48] Y. Yekutieli, R. Sagiv-Zohar, R. Aharonov, Y. Engel, B. Hochner, T. Flash, Dynamic model of the octopus arm. i. biomechanics of the octopus
405 reaching movement, *J Neurophysiol* 94 (2) (2005) 1443–1458.
- 406 [49] A. Kazakidi, V. Vavourakis, N. Pateromichelakis, J.A. Ekaterinaris, D.P. Tsakiris, Hydrodynamic analysis of octopus-like robotic arms, in:
407 IEEE Int Conf Rob Autom, ICRA 2012, St Paul, Minnesota, USA, 2012, pp. 5295–5300.
- 408 [50] I. Borazjani, L. Ge, F. Sotiropoulos, Curvilinear immersed boundary method for simulating fluid structure interaction with complex 3d rigid
409 bodies, *J Comput Phys* 227 (2008) 7587–7620.
- 410 [51] I. Borazjani, F. Sotiropoulos, E. D. Tytell, G. V. Lauder, Hydrodynamics of the bluegill sunfish c-start escape response: three-dimensional
411 simulations and comparison with experimental data, *J Exp Biol* 215 (2012) 671–684.
- 412 [52] M. Sfakiotakis, A. Kazakidi, N. Pateromichelakis, J.A. Ekaterinaris, D.P. Tsakiris, Robotic underwater propulsion inspired by the octopus
413 multi-arm swimming, in: IEEE Int Conf Rob Autom, (ICRA 2012), St Paul, Minnesota, USA, 2012, pp. 3833–3839.